Impact of Varying the Photoanode/Catalyst Interfacial Composition on Solar Water Oxidation: The Case of BiVO₄(010)/FeOOH Photoanodes

Adam M. Hilbrands,^{1,#} Shenli Zhang,^{2,#} Chenyu Zhou,^{3,#} Giacomo Melani,² Dae Han Wi,¹ Dongho Lee,¹ Zhaoyi Xi,^{3,4} Ashley R. Head,³ Mingzhao Liu,^{3,*} Giulia Galli,^{2,5,6*} and Kyoung-Shin Choi^{1,*}

Abstract

Photoanodes used in a water-splitting photoelectrochemical cell are almost always paired with an oxygen evolution catalyst (OEC) to efficiently utilize photon-generated holes for water oxidation because the surfaces of photoanodes are typically not catalytic for the water oxidation reaction. Suppressing electron-hole recombination at the photoanode/OEC interface is critical for the OEC to maximally utilize the holes reaching the interface for water oxidation. In order to explicitly demonstrate and investigate how the detailed features of the photoanode/OEC interface affect interfacial charge transfer and photocurrent generation for water oxidation, we prepared two BiVO₄(010)/FeOOH photoanodes with different Bi:V ratios at the outermost layer of the BiVO₄ interface (close to stoichiometric vs Bi-rich) while keeping all other factors in the bulk BiVO₄ and FeOOH layers identical. The resulting two photoanodes show a striking difference in the photocurrent onset potential and the photocurrent density for water oxidation. The ambient pressure X-ray photoelectron spectroscopy results show that these two BiVO₄(010)/FeOOH photoanodes show drastically different Fe²⁺:Fe³⁺ ratios in FeOOH both in dark and under illumination with water, demonstrating the immense impact of the interfacial composition and structure on interfacial charge transfer. Using computational studies, we reveal the effect of the surface Bi:V ratio on the hydration of the BiVO₄ surface and bonding with the FeOOH layer, which in turn affect the band alignments between BiVO₄ and FeOOH. These results explain the atomic origin of the experimentally observed differences in electron and hole transfer and solar water oxidation performance of the two photoanodes having different interfacial compositions.

¹Department of Chemistry, University of Wisconsin-Madison, Madison, WI 53706, United States

²Pritzker School of Molecular Engineering, University of Chicago, Chicago, IL 60637, USA

³Center for Functional Nanomaterials, Brookhaven National Laboratory, Upton, NY 11973, United States

⁴Department of Materials Science and Chemical Engineering, Stony Brook University, Stony Brook, NY 11794, United States

⁵Department of Chemistry, University of Chicago, Chicago, IL 60637, USA

⁶Argonne National Laboratory, Lemont, IL 60439, USA

[#]These authors contributed equally.

^{*} Correspondence and requests for materials should be addressed to M.L (email: mzliu@bnl.gov), G.G. (email: gagalli@uchicago.edu), and K.-S.C. (email: kschoi@chem.wisc.edu).

Introduction

In a water-splitting photoelectrochemical cell (PEC), a semiconductor electrode (photoelectrode) can directly utilize photon-generated charge carriers (electrons and holes) for water reduction and oxidation reactions. The band edge positions and work function of the photoelectrode affect the generation, separation, transport, and utilization of the photon-generated charge carriers for water-splitting reactions. In general, the surfaces of most photoelectrodes are not particularly catalytic for water reduction or water oxidation reactions. Thus, for the efficient utilization of surface reaching electrons and holes for water-splitting reactions the photocathode and photoanode are paired with a hydrogen evolution catalyst (HEC) and an oxygen evolution catalyst (OEC), respectively.³

In our recent study, we showed that when a ternary oxide containing two different metal ions, such as BiVO₄, is used as a photoanode, the surface metal composition (i.e., the surface Bi:V ratio) may not necessarily be the same as the bulk metal composition and can also be intentionally tuned.⁴ This can have an immense impact on the band edge positions and work function, even for the same facet exposed on the surface, thereby altering the band bending and the electron-hole separation at any given potential. This observation made us wonder how the variation of the surface composition of the same photoelectrode can impact the photoelectrode/catalyst junction when the same catalyst layer is deposited on the photoelectrode. We postulated that even when the same pair of photoelectrode and catalyst is selected, the details of the interfacial atomic composition and structure may affect the band alignments at the interface, influencing the interfacial electron-hole recombination and the overall solar-to-fuel conversion efficiency. We note that to the best of our knowledge, the impact of varying the interfacial structure formed between the same photoelectrode and catalyst pair on interfacial charge recombination has never been investigated prior to this work.

In our previous study establishing the impact of the surface Bi:V composition on the surface energetics of BiVO₄, we prepared and thoroughly characterized epitaxially grown BiVO₄(010) photoanodes with two different surface Bi:V ratios (i.e., close to stoichiometric and Bi-rich). Also, we identified theoretical BiVO₄ surface models that can closely mimic these two experimental surfaces by matching simulated scanning tunneling microscopy (STM) images from various surface models with the experimentally obtained STM images of the real samples.⁴ In the current study, using these previously well-established experimental and theoretical BiVO₄(010) surfaces with two different Bi:V surface ratios, we assembled BiVO₄/FeOOH photoanodes where FeOOH serves as an OEC. These two samples, composed of the identical BiVO₄ and FeOOH pair but different interfacial Bi:V compositions, offer an ideal opportunity to investigate the impact of the photoanode/catalyst interface on interfacial electron and hole transport. The two BiVO₄/FeOOH photoanodes show strikingly different photoelectrochemical oxygen evolution reaction (OER) performances, which is solely due to the difference at the BiVO₄/FeOOH interface. We performed computational as well as experimental investigations, including ambient pressure X-ray photoelectron spectroscopy (AP-XPS) under illumination with water, to probe interfacial charge transfer and band alignments between BiVO₄ and FeOOH. Using these results, we offer an atomic level understanding of how the BiVO₄/FeOOH interfacial composition and structure affect the interfacial band alignments and electron and hole transfer, directly impacting the OER performances.

Methods

Experimental Study

*Epitaxial BiVO*₄(010) *Film Preparation.* The epitaxial BiVO₄(010) thin film was deposited on commercial (100)-oriented yttrium-stabilized zirconia (YSZ) single-crystalline substrates (MTI Corp) by pulsed laser deposition (PLD) using a KrF excimer laser (λ = 248 nm) operated at a repetition rate of 20 Hz and a fluence of 1.8 J/cm² at the target, to ensure stoichiometric target-to-film elemental transfer. The ceramic target is prepared by pressing commercial BiVO₄ powder (Alfa Aesar, 99.9%, ~200 Mesh) into pellets and sintering them at 710 °C for 10 hours. A 50-nm-thick indium tin oxide (ITO) layer is epitaxially deposited over the YSZ substrates at 600 °C under a base pressure of 6 × 10⁻⁷ Torr as a conductive buffer layer. Subsequently, the BiVO₄ layer is grown at 675 °C in an oxygen atmosphere under a pressure of 2 × 10⁻² Torr.

The BiVO₄(010) thin film with a Bi-rich surface was prepared by immersing as-prepared BiVO₄ in a 15 mL 0.1 M NaOH (Sigma-Aldrich, 97%) solution for 1 min. The samples were then rinsed with deionized water (Barnstead GenPure Pro UV, resistivity >18 M Ω cm) and blow dried with air.

Photoelectrochemical deposition of FeOOH on BiVO₄. The photoelectrochemical deposition of FeOOH was adapted from a previous paper and adjusted for this study.⁵ The potentiostat, electrochemical set up, and light source used here are identical to those described in the photoelectrochemical characterization section with the addition of neutral density filters to the light source to adjust the light intensity on the BiVO₄ working electrode surface to 4 mWcm⁻². The plating solution was prepared by purging 60 mL of deionized water with N₂ for 1 hour to remove dissolved O₂ then adding 10 mM FeSO₄·7H₂O (Aldrich, 99%). The pH of the solution was 4.9. The FeOOH was deposited under illumination at a constant current of 10 µA/cm² for 50 s. corresponding to 0.5 mC/cm² of charge passed. During illumination photogenerated holes in the valance band of BiVO₄ are used to oxidize soluble Fe²⁺ to insoluble Fe³⁺ in a pH 4.9 solution, causing it to deposit as FeOOH onto the BiVO₄ surface. The electrical bias applied to maintain a current density of 10 µA/cm² creates an additional band bending at the BiVO₄ photoelectrode surface and facilitates the photoelectrochemical deposition of FeOOH. The electrodes were then rinsed with deionized water and blow dried. The applied current and charge passed were optimized for this study such that significant enhancement of water oxidation was seen after FeOOH deposition, but the FeOOH layer was thin enough that the surface Bi:V ratio of the underlying BiVO₄ layer can still be quantified by XPS.

Characterization. The morphology of the electrodes was examined by SEM (LEO 1530 microscope, Gemini) at an accelerating voltage of 2 kV. The crystallinity and orientation were confirmed using XRD (D8 Advance X-ray diffractometer, Bruker) using nickel-filtered copper $K\alpha$ -radiation with λ = 1.5418 Å. The optical absorbance of the electrodes was measured using a Cary 5000 ultraviolet–visible–near infrared spectrophotometer (Agilent) with an integrating sphere to simultaneously collect reflectance and transmittance from the electrodes. Transmission electron microscopy (TEM) images of BiVO₄/FeOOH samples were collected with a field emission transmission electron microscope (FEI Tecnai TF 30) operated at 300 kV. For the preparation of TEM samples, BiVO₄-FeOOH powders were obtained by scratching the films and the resulting powders were dispersed into ethanol. Then, the colloidal solution was drop-casted on a TEM grid (400 mesh copper grid supported with Lacey carbon, Electron Microscopy Sciences).

The Bi:V ratios of BiVO₄ and BiVO₄/FeOOH samples were measured by XPS (K-Alpha X-ray photoelectron spectrometer, Thermo Scientific) using monochromatized Al Kα X-ray (1486.6 eV) as the excitation source. The Bi 4f and V 2p core level spectra were obtained with a pass energy of 20 eV, and atomic percentages were calculated by integrating the peak areas using Avantage software (Thermo Scientific v.5.9919).

Photoelectrochemical characterization. All photoelectrochemical measurements were performed using an SP-200 potentiostat (Bio-Logic). An undivided 3-electrode cell was used with BiVO₄ as the working electrode, Pt as the counter electrode, and Ag/AgCl (4 M KCl) as the reference electrode. All potentials were converted to potential versus the reversible hydrogen electrode (RHE) using the following equation (where NHE is normal hydrogen electrode).

$$E(\text{vs RHE}) = E(\text{vs Ag/AgCl}) + E_{\text{Ag/AgCl}}(\text{RE}) + 0.0591 \text{ V} \times \text{pH}$$

$$(E_{\text{Ag/AgCl}}(\text{RE}) = 0.1976 \text{ V vs NHE at 25 °C})$$
(1)

Simulated solar light was generated using an LCS-100 solar simulator (Oriel Instruments) equipped with a 100 W Xe arc lamp (Newport) and an AM 1.5 G filter. An infrared filter (Newport) and a focusing lens were placed between the light source and the electrode, and the intensity of light was calibrated to 1 sun ($100 \, \text{mW/cm}^2$) at the back side of the BiVO₄ electrode using a National Renewable Energy Laboratory-certified GaAs reference cell (photovoltaic measurement). Photoelectrochemical J-V measurements were performed in a 0.5 M H₃BO₃ (Sigma-Aldrich, 99.5%) buffer solution in deionized water adjusted to pH 9.3 with KOH (Sigma-Aldrich, 85%). For sulfite oxidation measurements, 0.4 M Na₂SO₃ (Sigma-Aldrich, \geq 98%) was added to the 0.5 M borate buffer, and the final pH was 9.3. Photocurrent onset is reported as the open circuit potential in the given electrolyte under AM 1.5 G illumination where the photocurrent density is zero.

AP-XPS Studies. The chemical states of Fe, Bi, and V on the surfaces of the s-BiVO₄/FeOOH and Bi-BiVO₄/FeOOH photoelectrodes in dark, with water, and with water and light were examined by collecting Fe 2p, V 2p, and Bi 4f core level photoelectron spectra using an ambientpressure X-ray photoelectron spectroscopy instrument (AP-XPS) equipped with a differentially pumped hemispherical analyzer (SPECS PHOIBOS NAP 150) and a monochromatic Al K_α X-ray source (1486.6 eV). The base pressure is kept lower than 1×10^{-8} mbar. The measurement with water was carried out by dosing water, which is degassed by at least three consecutive freezepump-thaw cycles until no bubble evolves, into the XPS chamber at a pressure of 1.5 mbar. For the measurement with light, an ultraviolet lamp (Thorlab M365LP1 LED source, 365 nm) was installed on the XPS chamber window, and the light is focused on the sample by a convex lens. XPS results were calibrated by setting the binding energy of the Bi 4f7/2 peak to 159.0 eV⁶ and analyzed using CasaXPS software. While the C 1s peak (284.8 eV) from adventitious carbon contamination has been commonly used to calibrate the binding energies, due to the various and uncertain chemical nature of adventitious carbon (e.g., the ratio between C-C carbon and C-O carbon), the C 1s peak can be broad and may shift between samples, making it an unreliable reference. In this study, we take advantage of the presence of Bi³⁺ in our sample. The Bi 4f orbitals are drawn close to the atomic core and buried deeply in the electronic shell composed of 5d, 6s, and 6p orbitals. As a result, they are less affected by their chemical environment and typically produce sharp XPS spectral lines. Indeed, according to binding energy values available from the NIST database, a variety of bismuth oxides, including BiVO₄, Bi₂O₃, and NaBiO₃, all have the Bi 4f7/2 binding energy close to 159.0 eV.⁶ In the case of multi-peak fitting for each Fe 2p spectrum, we introduced a set of rigorous constraints on the fitting parameters. These constraints encompass peak area, peak distance, and peak width, all of which serve to minimize fitting errors. Specifically, the ratio of peak areas between 2p1/2 and 2p3/2 was constrained to maintain a 1:2 proportion. Additionally, we enforced equal values for the full width at half maximum (FWHM) of 2p1/2 and 2p3/2, not only within each doublet but also across all experimental conditions. Furthermore, the peak distance between 2p1/2 and 2p3/2 within each doublet was consistently constrained to be uniform across all experimental conditions. We note that the constraint parameters align well with the reported values in the literature.^{8,9}

Computational Methods

Our first-principles calculations were based on Kohn–Sham DFT and used the PBE functional, ¹⁰ as implemented in the Quantum ESPRESSO (v.7.0)^{11,12}code. We used norm-conserving pseudopotentials ^{13,14} with a 90 Ry energy cutoff, and a uniform k-point grid with 0.01 Å⁻¹ spacing for bulk cells and the same spacing, but only in the direction parallel to the interface, for slabs. Atomic forces were converged within 1 meV·Å⁻¹ for bulk configurations (see below for the criterion used for slabs). All calculations were spin-polarized and included a Hubbard term (U)¹⁵ correction to the *d* electrons of the transition metals (vanadium and iron). For vanadium sites in BiVO₄, we adopted U = 2.7 eV and validated against hybrid functional calculations in our previous work^{4,16} on the BiVO₄(010) surface. For irons sites in FeOOH, we used U = 3.5 eV to best match the structural, electronic, and magnetic properties obtained in experiments. Specifically, our calculated lattice parameters of γ -FeOOH (a=3.919 Å, b=12.602 Å and c=3.131 Å) are within 2% of the experimental measurements^{17,18}. We obtained a band gap of 1.8 eV that is close to the experimentally measured band gap 2.06 eV,¹⁷ and an anti-ferromagnetically (AFM) ordered ground state, consistent with experiments^{17,19} and previous computational studies.^{20,21}

Atomistic models of BiVO₄ and FeOOH surfaces. To build atomistic slab models of dry BiVO₄ interfaced with FeOOH, we used the stoichiometric and Bi-rich BiVO₄(010) surface structures adopted in our previous work. We then generated hydrated BiVO₄ surface structures by extracting representative snapshots from First-Principles Molecular Dynamics (FPMD) simulations of BiVO₄ interfaced with liquid water after equilibration. Liquid water was represented with 64 water molecules. FPMD simulations were carried out at finite temperature (330 K) using the Qbox code (versions 1.75.0 and 1.74.2), employing the SCAN functional²² and norm-conserving pseudopotentials^{13,14} with a kinetic-energy cutoff of 80 Ry. Details of these simulations will be reported elsewhere. The hydrated stoichiometric (010) model used in this work consists of both molecularly adsorbed and dissociatively adsorbed water on the BiVO₄ surface, with molecular adsorbates being more abundant, given their relative energetic stability, in agreement with previous theoretical studies.^{23–25} The Bi-rich model is built starting from a stoichiometric one, following a procedure that mimics experimental conditions. In experiments⁴ the Bi-rich BiVO₄ surface is obtained by treating a sample with a stoichiometric surface with a 0.1 M NaOH solution, which strips away the top-most vanadium layer. The resulting Bi-rich surface obtained in a strongly basic solution is most likely hydroxylated. Hence, to computationally model the Bi-rich surface, we considered a stoichiometric slab terminated by four Bi(OH)₃ groups.

Finally, since all of our electronic structure calculations were carried out at the PBE+U level of theory, we further relaxed (i.e., we further optimized the atomistic configurations of) the snapshots extracted from FPMD simulations at the PBE+U level of theory with the Quantum ESPRESSO code; atomic forces were converged within 100 meV·Å⁻¹. For stoichiometric BiVO₄ slabs, a monolayer of molecularly adsorbed water as well as dissociatively adsorbed water were kept on the surface, and the remaining water molecules present in FPMD simulations were removed. For Bi-rich BiVO₄ slabs, the surface was terminated by four Bi(OH)₃ groups and all the water molecules present in FPMD simulations were removed.

In the case of γ -FeOOH, we used a layered crystal structure¹⁷ along the [010] crystallographic direction, and the (010) surface could be directly obtained without any further treatment. In addition, the (010) surface is naturally terminated by OH groups, and thus no further hydroxylation was considered. For surface calculations in contact with vacuum, we used a 2x2x3 supercell (the 2x in the in-plane direction is necessary to describe the AFM ordering) and included 40 Å of vacuum; we checked the convergence of the band alignment with respect to slab and vacuum thickness. The slab was relaxed with forces converged within $100 \text{ meV} \cdot \text{Å}^{-1}$.

Atomistic models of FeOOH-BiVO₄ heterostructures. In our model heterostructures, we included 6 atomic layers of BiVO₄ and 10 atomic layers of FeOOH. All the interfaces were formed between BiVO₄(010) and FeOOH(010) surfaces and all the heterostructures were relaxed with forces converged within 100 meV·Å⁻¹. For the stoichiometric case without hydration, we used the p2pint code²⁶ to generate four FeOOH-BiVO₄ heterostructures with different Fe-O-Bi bond angles and bond distances by rotating the FeOOH(010) surface with respect to the BiVO₄(010) surface around the [010] axis by different angles, and by translating the two BiVO₄ and FeOOH(010) surfaces relative to each other. We used the in-plane lattice parameters of the BiVO₄ slab to construct the heterostructures: in experiments, BiVO₄ serves as the substrate for FeOOH growth, and thus BiVO₄ is not strained, while FeOOH is expected to be. For the Bi-rich case without hydration, we generated one heterostructure with the same procedure outlined above. For the hydrated stoichiometric and Bi-rich heterostructures, we adopted the same in-plane lattice parameters as in the non-hydrated cases, and we substituted the dry Bi-rich BiVO₄(010) surface with the corresponding hydrated BiVO₄(010) surface model.

Calculation of band alignments. We computed the band alignments between BiVO₄ and FeOOH using two different methodologies, which in all cases gave consistent results: (i) electrostatic potential (EP) alignment^{27,28} and (ii) calculation of the local density of states (LDOS). ^{29,30} We applied method (i) to obtain the band alignments both before and after contact and method (ii) to obtain the band alignments after contact. To obtain the band alignments before contact with method (i), we calculate the energy (ε_{slab}) of the CBM and VBM of each slab model relative to vacuum, according to the following equations:

$$\varepsilon_{\rm slab}^{\rm CBM} = \varepsilon_{\rm bulk}^{\rm CBM} + \Delta V_{\rm slab}^{\rm vac} = \varepsilon_{\rm bulk}^{\rm CBM_{abs}} - \overline{V}_{\rm bulk} + \overline{V}_{\rm slab} - V_{\rm slab}^{\rm vac} \tag{2}$$

$$\varepsilon_{\text{slab}}^{\text{VBM}} = \varepsilon_{\text{bulk}}^{\text{VBM}} + \Delta V_{\text{bulk}}^{\text{vac}} = \varepsilon_{\text{bulk}}^{\text{VBM}_{\text{abs}}} - \overline{V}_{\text{bulk}} + \overline{V}_{\text{slab}} - V_{\text{slab}}^{\text{vac}}$$
(3)

In eqs. 2-3, $\varepsilon_{\rm bulk}^{\rm CBM}$ and $\varepsilon_{\rm bulk}^{\rm VBM}$ are the band edge positions computed with respect to the average electrostatic potential of the bulk semiconductor in a periodic supercell, calculated as $(\varepsilon_{\rm bulk}^{\rm VBM/CBM}_{\rm abs} - \overline{\rm V}_{\rm bulk})$, and $\varepsilon_{\rm bulk}^{\rm VBM/CBM}_{\rm abs}$ is the absolute value of the energy of the CBM and VBM

computed for the bulk phase; \overline{V}_{bulk} is the average electrostatic potential of the bulk phase, where we used the pristine bulk structure of BiVO₄ and FeOOH for our calculations; ΔV_{bulk}^{vac} is the electrostatic potential of the material relative to vacuum and can be obtained in each slab model in contact with vacuum as: $\overline{V}_{slab} - V_{slab}^{vac}$. Here \overline{V}_{slab} is the averaged electrostatic potential in the slab model, computed in the bulk region, and V_{slab}^{vac} is the vacuum level in that slab model, where in our calculations we included a dipole correction if dipole moments were present on the surface.

To obtain \overline{V}_{slab} , we first calculated a planar average of the potential (V) perpendicular to the slab surface using eq. 4 below and then applied a windowing average to obtain \overline{V}_{slab} using eq. 5.

$$\bar{V}(z) = \frac{1}{A_{xy}} \int dx dy \, V(x, y, z) \tag{4}$$

$$\bar{\mathbf{V}}_{\text{slab}} = \frac{1}{2l} \int_{-l}^{l} dz \, \bar{V}(z) \tag{5}$$

In eqs. 4-5, V(x, y, z) is the electrostatic potential arising from atomic nuclei and valence electrons; A_{xy} is the area of the plane parallel to the surface in our slab model, and l is the spacing we chose along the axis perpendicular to the surface to obtain the average, which is taken within the bulk-like region of the slab.

The band edge positions of FeOOH (100) shown in **Figure 5b** were obtained by using the differences between the band edges of the (010) and (100) facets of FeOOH, as reported in a previous study.³¹

The band alignment of the two oxides after contact is obtained by lining up the average electrostatic potential of the two materials in the heterostructure. The conduction and valence band offsets between the two materials (CBO and VBO, respectively) were calculated using the following equations:

$$CBO = \varepsilon_{\text{bulk-BVO}}^{CBM} - \varepsilon_{\text{bulk-FeOOH}}^{CBM} + \Delta V_{\text{hetero}}$$
 (6)

$$VBO = \varepsilon_{\text{bulk-BVO}}^{\text{VBM}} - \varepsilon_{\text{bulk-FeOOH}}^{\text{VBM}} + \Delta V_{\text{hetero}}$$
 (7)

In eqs. 6 and 7, $\varepsilon_{\text{bulk-BVO}}^{\text{CBM/VBM}}$ are the respective quantities entering eq.2, and the calculations for bulk FeOOH were conducted for the atomic structure (and lattice constant) corresponding to the bulk-like region of FeOOH in the heterostructure, so as to include strain and possible structural distortion effects caused by the interface. ΔV_{hetero} is the average electrostatic potential difference between BiVO₄ and FeOOH regions in the heterostructure computed in their corresponding bulk-like regions in the heterostructure using eqs.4 and 5.

The method based on LDOS calculations (method (ii) above) evaluates the band offset between the two materials using the following equations:

$$CBO = \varepsilon_{BVO}^{CBM} - \varepsilon_{FeOOH}^{CBM}$$
 (8)

$$VBO = \varepsilon_{BVO}^{VBM} - \varepsilon_{FeOOH}^{VBM} \tag{9}$$

In eqs. 8-9, $E^{\text{CBM/VBM}}$ are the CBM (VBM) in the bulk-like BiVO₄ and FeOOH regions in the heterostructure.

The LDOS in the direction z perpendicular to the interface is defined as:

$$D(\varepsilon, z) = 2\sum_{n} |\langle z|\psi_{n} \rangle|^{2} \delta(\varepsilon - \varepsilon_{n})$$
(10)

In eq. 10, $|\langle z|\psi_n\rangle|^2$ is the square modulus of the single particle wavefunction ψ_n integrated in the xy plane parallel to the interface, and the factor of 2 accounts for spin degeneracy; ε_n is the Kohn-Sham eigenvalue corresponding to the wavefunction ψ_n . We used the abinitioToolKit code,³² which implements eq. 10 to obtain the band alignment after contact.

We found that for the hydrated stoichiometric BiVO₄/FeOOH heterostructure, LDOS calculations yielded inaccurate results (that is values of the band edges showing oscillations over z that were too large to obtain accurate results). Therefore, we applied only method (i). In all other cases we applied methods (i) and (ii) and obtained consistent results.

Results and Discussion

The crystal structure of monoclinic scheelite BiVO₄ can be Synthesis and characterization. reported as an I-centered cell or a C-centered cell and the (hkl) indices of BiVO₄ used in this study are with respect to the C-centered monoclinic cell (C 2/c)^{4,33}. The epitaxial BiVO₄(010) films used in this study were prepared by pulsed laser deposition following the procedure published previously^{4,34}. Yttrium-stabilized cubic zirconia (YSZ) was used as the substrate after coating the surface with a thin epitaxial layer of indium tin oxide (ITO) to make the substrate electrically conductive. The Bi:V ratios of the as-deposited BiVO₄(010) determined by X-ray photoelectron spectroscopy (XPS) and low energy ion scattering spectroscopy (LEIS)⁴ were 47:53 and 43:57, respectively. While the surface is slightly V-rich, the surface Bi:V ratio of the as-deposited BiVO₄(010) film is very close to 1:1. Thus, we will refer to this sample as stoichiometric BiVO₄ (s-BiVO₄ in short) in this study. In our previous study, we reported a simple base-treatment method that can remove V only from the outermost layer with negligible change in the underlying bulk BiVO₄ layer.⁴ After the base treatment, the surface Bi:V ratio determined by LEIS is 79:21.⁴ Owing to its sampling depth limited to the sample's first atomic layer, LEIS has a unique capability to quantify the atomic ratio of only the outermost layer of the sample. 35,36 The Bi:V ratio determined by X-ray photoelectron spectroscopy (XPS), which has deeper probing depth than LEIS was 53:47.4 The fact that the Bi:V ratio determined by XPS is still very close to 1:1 indicates that the V etching by the base-treatment is limited only to the outermost layer without affecting the Bi:V ratio in the underlying bulk layer. This base-treated sample is denoted as Bi-rich BiVO₄ (Bi-BiVO₄ in short) in this study. The fact that these two samples differ only in the metal composition in the outermost layer while having all other features the same (e.g., crystallinity, absorbance, surface roughness) was carefully confirmed and reported in our previous study.⁴

Onto these two different BiVO₄(010) photoelectrodes (s-BiVO₄ and Bi-BiVO₄), an FeOOH OEC layer was photoelectrochemically deposited, producing s-BiVO₄/FeOOH and Bi-BiVO₄/FeOOH photoelectrodes having different BiVO₄/FeOOH interfacial structures; the former has an FeOOH layer deposited on the stoichiometric BiVO₄ surface, and the latter has an FeOOH layer deposited on the Bi-rich BiVO₄ surface. FeOOH was used as an OEC because among earth-abundant transition metal oxyhydroxide-based OECs composed of a single metal, FeOOH is the most efficient, stable, and inexpensive OEC.³⁷ (The use of mixed metal oxyhydroxides was avoided to simplify computational modeling.) Also, FeOOH has been demonstrated to interface well with BiVO₄ to enhance photocurrent for OER.^{5,38}

The anodic electrodeposition mechanisms of FeOOH³⁹ and the use of photogenerated holes in BiVO₄ for the photoelectrochemical anodic deposition of FeOOH are explained in detail elsewhere.^{5,38,40,41} The charges passed to deposit an FeOOH layer on the stoichiometric and Birich BiVO₄ photoelectrodes were regulated to be the same. As the goal of this study is not to optimize the thickness of the FeOOH to maximize the OER performance of the resulting BiVO₄/FeOOH film but to investigate the impact of the BiVO₄ surface composition on the BiVO₄/FeOOH interfacial structure and the overall OER performance of the resulting BiVO₄/FeOOH photoelectrodes, the thickness of the FeOOH was regulated to be thin enough to allow for the investigation of the underlying BiVO₄ surface by XPS. Having a thin FeOOH layer also ensures a greater contribution from the first atomic FeOOH layer (the layer in direct contact with BiVO₄) to the composition and property of the entire FeOOH layer.

The XRD patterns of the s-BiVO₄/FeOOH and Bi-BiVO₄/FeOOH electrodes before and after FeOOH deposition show no difference (**Figure 1a-c**), suggesting that the FeOOH is extremely thin and/or amorphous. Also, the absorbance of s-BiVO₄/FeOOH and Bi-BiVO₄/FeOOH before and after FeOOH deposition shows no difference, indicating that the FeOOH layer is extremely thin and that the photons absorbed by the s-BiVO₄/FeOOH and Bi-BiVO₄/FeOOH photoelectrodes during photocurrent measurement will be the same (**Figure 1d**). The TEM images of the s-BiVO₄/FeOOH and Bi-BiVO₄/FeOOH electrodes show that the BiVO₄ surfaces are uniformly covered by FeOOH and the thickness of the FeOOH layer on both electrodes is ~ 5 nm (**Figure 1e-f**). As the FeOOH layer is thin and uniform, no noticeable difference on the surface morphology or roughness was observed in their scanning electron microscopy (SEM) images (**Figure S1**). These results confirm that any difference obtained by these two photoelectrodes for photoelectrochemical water oxidation will solely be due to the difference in the BiVO₄/FeOOH interfacial structure.

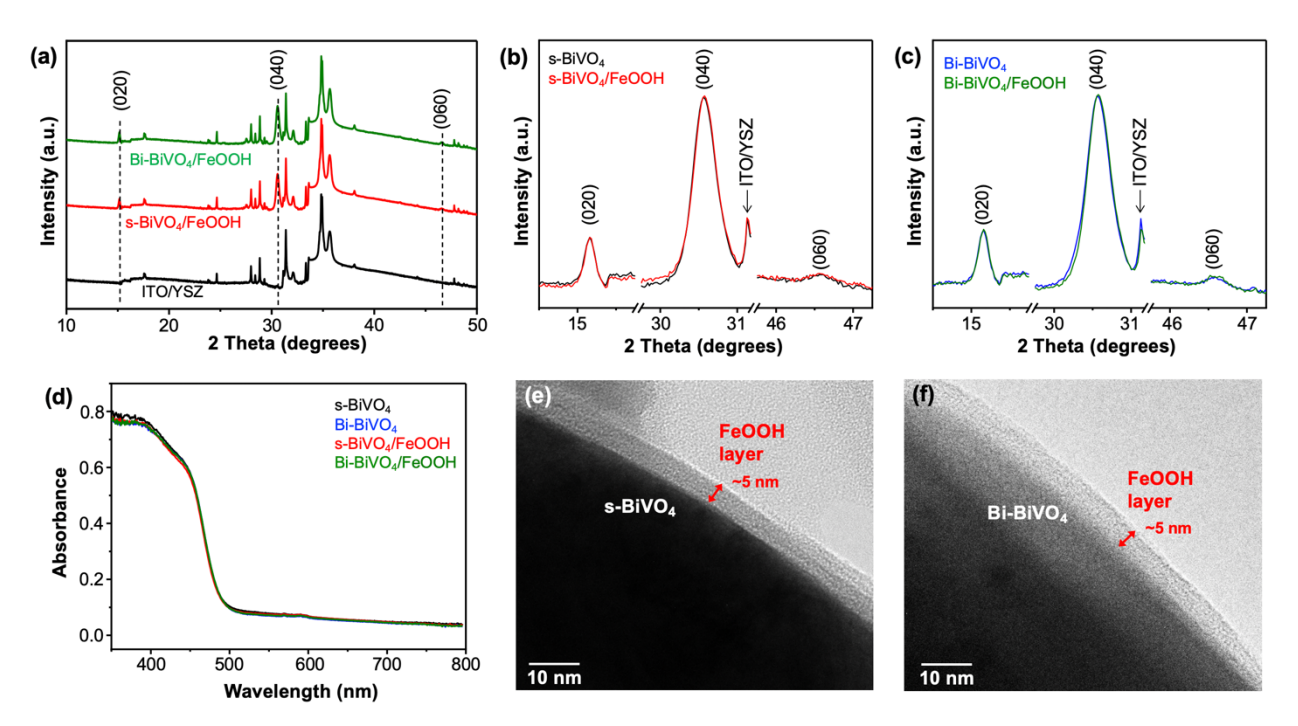


Figure 1. (a) XRD patterns of s-BiVO₄/FeOOH (red) and Bi-BiVO₄/FeOOH (green) electrodes (JCPDS 14-0688) with (0k0) peaks confirming the epitaxial (010) nature of the BiVO₄ film. XRD

pattern of the ITO/YSZ substrate is shown in black. No FeOOH peaks were observed. Magnification of (0k0) diffraction peaks of (b) s-BiVO₄ and (c) Bi-BiVO₄ before and after FeOOH deposition showing no differences. (d) UV-vis spectra of s-BiVO₄ and Bi-BiVO₄ before and after FeOOH deposition showing no differences. Representative TEM images of (e) s-BiVO₄/FeOOH and (f) Bi-BiVO₄/FeOOH showing a conformally coated, ~5 nm thick FeOOH layer on BiVO₄.

Photoelectrochemical properties. The J-V plots obtained with s-BiVO₄, Bi-BiVO₄, s-BiVO₄/FeOOH and Bi-BiVO₄/FeOOH for photoelectrochemical water oxidation in 0.5 M borate buffer (pH 9.3) under AM 1.5G, 100 mW/cm² illumination are shown in **Figure 2a**. When FeOOH is absent, the OER performances of s-BiVO₄ and Bi-BiVO₄ photoelectrodes are equally poor with Bi-BiVO₄ showing only a slightly better performance. For example, no photocurrent appeared below 0.7 V vs RHE and the photocurrent densities at 1.2 V vs. RHE are below 0.5 mA/cm² for both samples.

In our previous study, we showed that the Bi-BiVO₄ photoelectrode has more favorable interfacial energetics (e.g., band edges and the Fermi level closer to vacuum) to create more band bending at any given applied potential and can separate more electron-hole pairs and send more holes to the surface. This was confirmed by a strikingly higher photocurrent density generated by Bi-BiVO₄ for sulfite oxidation. (Owing to the fast sulfite oxidation kinetics, sulfite oxidation can convert all surface reaching holes to anodic photocurrent without losing them to surface recombination.) However, the same difference is not shown for water oxidation because the water oxidation kinetics on the bare BiVO₄ surfaces (whether stoichiometric or Bi-rich) are very slow and the majority of the surface reaching holes are lost to surface recombination before being used to generate photocurrent for OER.

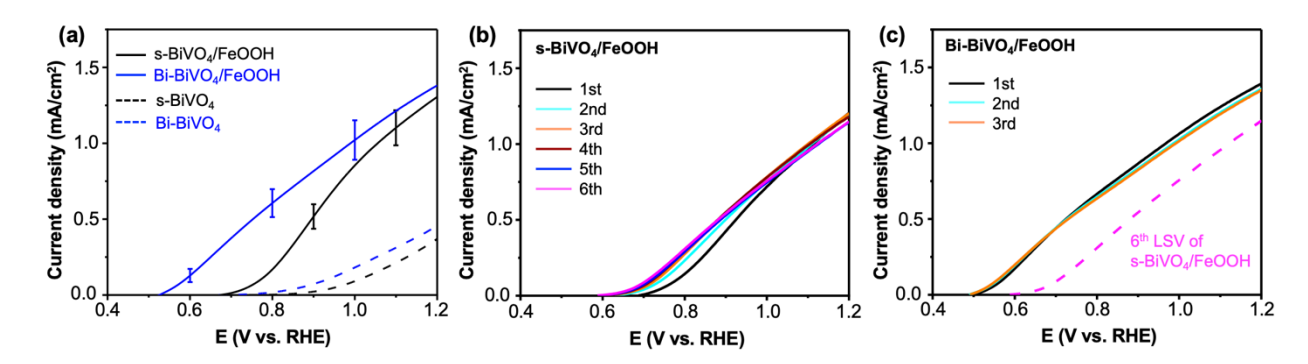


Figure 2. (a) J-V plots for OER of s-BiVO₄, Bi-BiVO₄, s-BiVO₄/FeOOH and Bi-BiVO₄/FeOOH photoelectrodes; each curve is obtained by averaging the J-V plots of five individual samples. The error bars represent standard deviations of the average current densities at selected potentials. The J-V plots were recorded in 0.5 M borate buffer (pH 9.3) under AM 1.5G, 100 mW/cm² illumination. Repeated J-V measurements of (b) s-BiVO₄/FeOOH and (c) Bi-BiVO₄/FeOOH photoelectrodes under the same conditions.

When a 5 nm thick FeOOH layer is present, a remarkable increase in photocurrent was observed for both samples. Another critical feature to note is that the performance difference between s-BiVO₄/FeOOH and Bi-BiVO₄/FeOOH is far greater than that of s-BiVO₄ and Bi-BiVO₄.

As s-BiVO₄/FeOOH and Bi-BiVO₄/FeOOH are composed of the same photoelectrode and the same OEC, the observed OER performance difference is unarguably due to the difference in the BiVO₄/FeOOH interface, and this result demonstrates the immense impact of the photoelectrode's outermost composition at the photoelectrode/OEC interface on the interfacial hole transfer. For example, the onset of Bi-BiVO₄/FeOOH is $(0.52 \pm 0.02 \text{ V vs RHE})$ while the onset of s-BiVO₄/FeOOH is $(0.66 \pm 0.02 \text{ V vs RHE})$ with a difference of 0.14 V. The photocurrent density at 0.7 V vs. RHE is $0.38 \pm 0.07 \text{ mA/cm}^2$ for Bi-BiVO₄/FeOOH, and it is only $0.02 \pm 0.01 \text{ mA/cm}^2$ for s-BiVO₄/FeOOH. The observed performance difference decreases as a more positive potential (> 1.0 V vs RHE) is applied, which creates more band bending and aids electron-hole separation. We note that the performance in the low-bias region is the most important for photoelectrochemical application where the goal is to utilize solar energy to minimize the external voltage input needed to drive reactions.

In our previous study comparing s-BiVO₄ and Bi-BiVO₄ for sulfite oxidation, we discovered that the surface composition of s-BiVO₄ changes when the J-V measurement was repeated due to V leaching during the J-V measurement, which caused the Bi:V ratio to keep increasing.⁴ As the surface Bi:V ratio increased, the photocurrent kept increasing until the Bi:V ratio became similar to that of Bi-BiVO₄ (it converged at the 7th J-V measurement), which was stable in the given electrolyte. In contrast, the surface Bi:V ratio of the Bi-BiVO₄ sample and its J-V plots did not change much during the repeated measurements because it already contained a Bi-rich surface that was stable in the given electrolyte. Thus, we also repeated the J-V measurement of the s-BiVO₄/FeOOH and Bi-BiVO₄/FeOOH photoelectrodes for OER to examine whether the Bi:V ratios or their OER performances change during repeated J-V measurements. We predicted that the surface Bi:V ratio of the s-BiVO₄/FeOOH and therefore its OER performance should not change because unlike bare s-BiVO₄, the surface of s-BiVO₄ is interfaced with FeOOH, which should prevent facile V leaching. Indeed, Figure 2b shows that the photocurrent density of s-BiVO₄/FeOOH increases only slightly during the first two J-V measurements and converges after the 3rd J-V measurement. This slight increase in the photocurrent density is most likely due to regions where the s-BiVO₄ surface is not completely covered by FeOOH, allowing V to leach out until the equilibrium Bi:V surface ratio in the given pH is established. The fact that the photocurrent increase is not significant and the photocurrent converges within 3 cycles suggests that the pinhole area is limited. The results obtained from repeated J-V measurements of Bi-BiVO₄/FeOOH are shown in Figure 2c. The J-V plot of Bi-BiVO₄/FeOOH does not change much during repeated measurements, and it remains significantly superior to the converged J-V plot of s-BiVO₄/FeOOH. After the convergence of the J-V plots, s-BiVO₄/FeOOH still has a slightly V-rich interface (Bi:V ratio of 49:51) while Bi-BiVO₄/FeOOH still has a Bi-rich interface (Bi:V ratio of 53:47) according to the XPS results. (The LEIS measurement is no longer possible due to the presence of FeOOH.) These results show that the surface compositions of BiVO₄ at the BiVO₄/FeOOH interface, which is stabilized by the presence of FeOOH, are more stable and can have a longer-lasting impact than the surface compositions of the bare BiVO₄ surfaces where all V at the outermost layer can be readily leached out in basic media.

AP-XPS study. The differences in the BiVO₄/FeOOH junction in s-BiVO₄/FeOOH and Bi-BiVO₄/FeOOH photoelectrodes were probed by comparing the Fe 2p XPS spectra measured in the dark and under illumination with water. The FeOOH on BiVO₄ was prepared by photodeposition where photogenerated holes in BiVO₄ are used to oxidize soluble Fe²⁺ to insoluble Fe³⁺ in a pH

4.9 solution, and the resulting insoluble Fe³⁺ is precipitated out as FeOOH on BiVO₄. As the same number of holes was consumed on s-BiVO₄ and Bi-BiVO₄ to produce Fe³⁺ (i.e., constant current deposition) and only insoluble Fe³⁺ can be deposited as FeOOH, the FeOOH layer was deposited with the same thickness on s-BiVO₄ and Bi-BiVO₄ as shown in **Figure 1 e-f**. However, when the photodeposition is completed and the BiVO₄/FeOOH samples rest under the open circuit condition, the Fermi levels of BiVO₄ and FeOOH in the resting state equilibrate by transferring electrons from the phase with a higher Fermi level to the phase with a lower Fermi level. If electrons transferred from BiVO₄ to FeOOH during this process localize on Fe³⁺ at the interface, Fe²⁺ would form. Therefore, the Fe²⁺:Fe³⁺ ratio in the FeOOH layer under the open circuit condition in the dark allows us to deduce the charge transfer that had to occur between the BiVO₄ and FeOOH to establish an equilibrium at the interface.

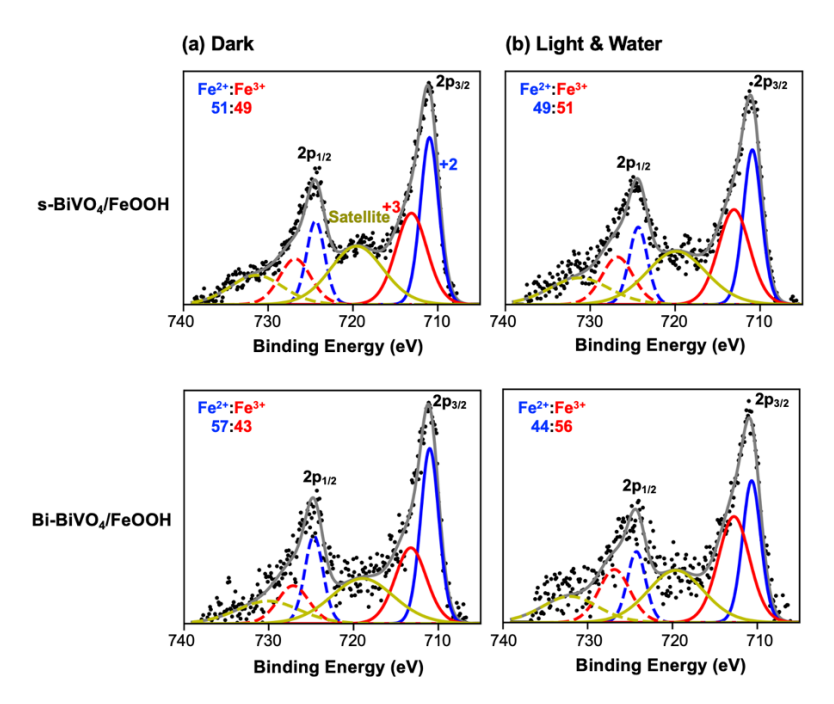


Figure 3. Fe 2p XPS Spectra of (top) s-BiVO₄/FeOOH and (bottom) Bi-BiVO₄/FeOOH: (a) in dark and (b) under illumination with water. The experimentally obtained peaks (black dotted lines) are deconvoluted to Fe^{2+} (blue), Fe^{3+} (red), and satellite (olive green) peaks (solid lines for $2p_{3/2}$ and dashed lines for $2p_{1/2}$). The sum of the fitted peaks is shown as a gray line. The Fe^{2+} : Fe^{3+} ratio for each case is shown in the figure.

The position of the Fe 2p XPS peaks are sensitive to the oxidation states of Fe and therefore the Fe²⁺: Fe³⁺ ratio in the FeOOH layer can be quantified by peak fitting. Also, as the FeOOH in these samples is extremely thin, the XPS probing depth can reach the BiVO₄ surface, meaning that the Fe²⁺: Fe³⁺ ratio obtained by XPS represents the averaged Fe²⁺: Fe³⁺ ratio throughout the entire FeOOH layer with a significant contribution from the interfacial Fe²⁺: Fe³⁺ ratio. **Figure 3a** shows the peak fitting of Fe 2p XPS spectra obtained under the open circuit condition in the dark, which shows a difference in the Fe²⁺:Fe³⁺ ratio of the FeOOH layer on the two different BiVO₄ surfaces. The Fe²⁺:Fe³⁺ ratio in FeOOH of s-BiVO₄/FeOOH is 51:49 while that of Bi-BiVO₄/FeOOH is 57:43. These results suggest that the Bi-BiVO₄ surface is more reducing and more electrons are

transferred from Bi-BiVO₄ to FeOOH than from s-BiVO₄ to FeOOH when establishing the interfacial equilibrium. In fact, our previous study showed experimentally and computationally that the Bi-BiVO₄ surface has a work function closer to vacuum than the s-BiVO₄ surface, although the bulk BiVO₄ regions in these two samples are the same.⁴ Thus, when these two BiVO₄ electrodes interface with the same FeOOH, it is expected that more electrons are transferred from Bi-BiVO₄ to the FeOOH layer than from s-BiVO₄ to the FeOOH layer. The schematic band alignments inferred from the previous study⁴ and the Fe XPS results obtained in the dark are shown in **Figure 4a-b**; the higher Fermi level of Bi-BiVO₄ transferring more electrons to FeOOH to establish an equilibrium results in more band banding and a higher Fe²⁺:Fe³⁺ ratio in the FeOOH layer.

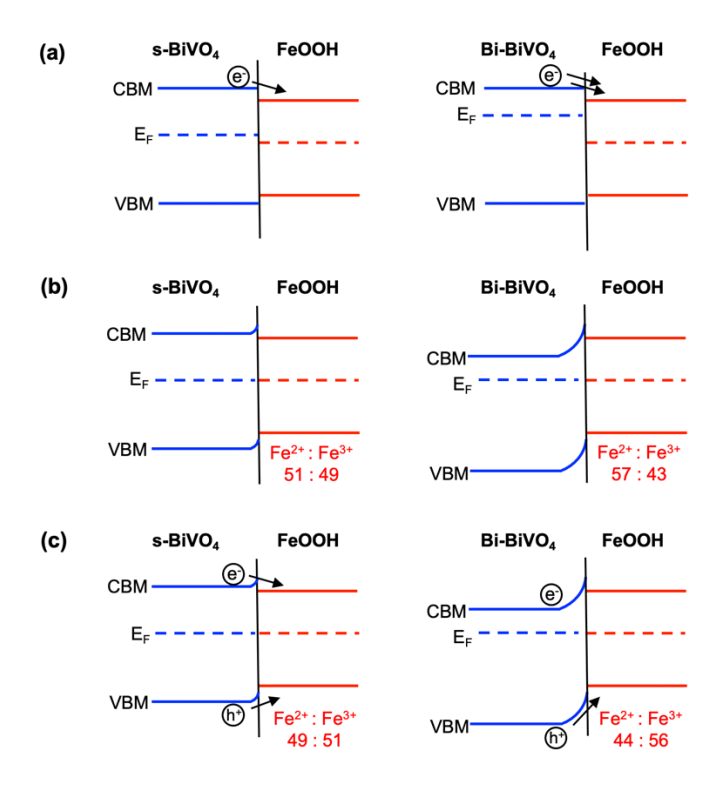


Figure 4. Schematic diagrams showing the interfacial band alignment of s-BiVO₄/FeOOH and Bi-BiVO₄/FeOOH (a) under the open circuit condition in the dark before equilibrium, (b) under the open circuit condition in the dark after equilibrium, and (c) under illumination with water under the open circuit condition.

Next, we introduced UV illumination (365 nm, LED light) and water (i.e., 1.5 mbar of water vapor) to these samples under the open circuit condition and obtained the Fe 2p spectra using AP-XPS. No considerable change in the Fe²⁺:Fe³⁺ ratio was observed for the s-BiVO₄/FeOOH sample (**Figure 3b**). In contrast, the Fe²⁺:Fe³⁺ ratio in FeOOH of Bi-BiVO₄/FeOOH decreased notably from 57:43 to 44:56 (**Figure 3b**). When the photoelectrodes are illuminated, electron-hole pairs are generated in the BiVO₄ layer by photon absorption. (The photon absorption by FeOOH is negligible as shown in **Figure 1d**). If all electron-hole pairs generated in the BiVO₄ layer rapidly recombine in BiVO₄, or both electrons and holes are injected to FeOOH to recombine in FeOOH,

no change in the Fe²⁺:Fe³⁺ ratio in FeOOH would result. However, if only one type of photogenerated charge carriers (electrons or holes) are primarily injected to the FeOOH layer and localized on Fe²⁺ or Fe³⁺ before they eventually recombine, the Fe²⁺:Fe³⁺ ratio in FeOOH during the in-situ AP-XPS measurement would change. The fact that the Fe²⁺:Fe³⁺ ratio in FeOOH of s-BiVO₄/FeOOH does not change during illumination means that the band alignment at the BiVO₄/FeOOH interface does not promote selective electron or hole transfer from s-BiVO₄ to FeOOH under illumination (**Figure 4c**). In contrast, the fact that the Fe³⁺ amount in FeOOH of Bi-BiVO₄/FeOOH increases during illumination means that the band alignment at the Bi-BiVO₄/FeOOH interface selectively promotes hole transfer from Bi-BiVO₄ to the FeOOH under illumination (Figure 4c). We note that n-type BiVO₄/FeOOH serves as a photoanode where holes are transferred to FeOOH to be used for OER. Thus, the Bi-BiVO₄/FeOOH sample with the interfacial band alignment that can selectively promote hole transfer from Bi-BiVO₄ to FeOOH can suffer less from electron-hole recombination than s-BiVO₄/FeOOH during PEC operation. This means Bi-BiVO₄/FeOOH will have an earlier photocurrent onset for OER and generate more photocurrent for OER at any given potential than s-BiVO₄/FeOOH until a significantly positive bias is applied to separate all electron-hole pairs in BiVO₄. This agrees well with J-V plots of s-BiVO₄/FeOOH and Bi-BiVO₄/FeOOH for OER shown in Figure 2a.

The schematic band alignments at the s-BiVO₄/FeOOH and Bi-BiVO₄/FeOOH interfaces shown in **Figure 4** are based on our macroscopic consideration of the work functions of s-BiVO₄ and Bi-BiVO₄⁴ and Fe XPS results of the s-BiVO₄/FeOOH and Bi-BiVO₄/FeOOH. Next, we performed computational investigations using atomistic slab models of BiVO₄ and FeOOH to elucidate how the surface composition of BiVO₄ affects the structure and bonding at the BiVO₄/FeOOH interfaces at an atomic level and how they impact the band alignment, which will allow us to understand a microscopic-level origin of the observed differences in interfacial charge transfer and photocurrent generation.

Computational study. We first computed the band edge positions of BiVO₄(010) and FeOOH before contact, which were obtained in separate slabs in contact with vacuum. For BiVO₄, we considered two surface conditions for both s-BiVO₄(010) and Bi-BiVO₄(010) (Figure 5a): dry surfaces and hydrated surfaces. For the dry surfaces of s-BiVO₄ and Bi-BiVO₄, we used the surface models from our previous study, whose resemblance to the surfaces of the experimental epitaxial samples was verified using simulated and experimental STM images. The hydrated surface of s-BiVO₄ was obtained by adding a monolayer of water molecule to the surface. The resulting atomistic model is shown in **Figure 6a**. As revealed by our First-Principle Molecular Dynamics simulations (FPMD) and a previous study,²³ hydroxylation of the surface, which requires dissociative water adsorption, is not energetically favorable on the stoichiometric BiVO₄ surface. Thus, our atomistic model of the hydrated s-BiVO₄ surface (Figure 6a) mostly consists of water molecules adsorbed non-dissociatively (i.e., adsorbed as water molecules) on the surface Bi atoms with only a small portion of water adsorbed dissociatively and hydroxylating the surface Bi (marked with blue circles). The adsorbed water molecules are hydrogen bonded to the O atoms of the s-BiVO₄ surface. We note that the top and bottom hydrated BiVO₄ slabs in **Figure 6a** show slightly different hydrated configurations, as they are snapshots extracted from a FPMD simulations at finite T. The vibrational motion of the surface atoms of the hydrated surface model at finite T results in the fluctuation of the band edge positions, which is represented as shaded boxes at the CBM and VBM in Figure 5a.

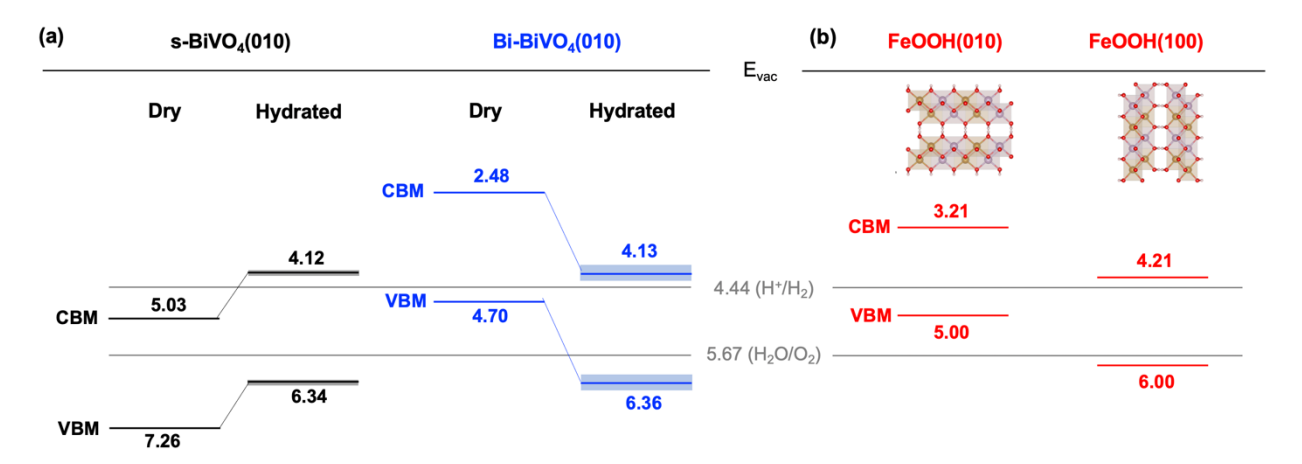


Figure 5. The conduction band minimum (CBM) and valence band maximum (VBM) of (a) s-BiVO₄(010) and Bi-BiVO₄(010) and (b) FeOOH(010) and FeOOH(100) before contact. Their positions with respect to the vacuum level (E_{vac}) are shown in eV. Electronic structure calculations were carried out at the DFT+U level of theory. The shaded region in correspondence of the CBM and VBM of the hydrated BiVO₄ models represents the fluctuation of the band edge positions at finite T and the average values of the band position is shown as an indicative figure.

The hydrated Bi-BiVO₄ surface was obtained by fully hydroxylating all Bi atoms on the surface (**Figure 6b**), considering the experimental condition used to prepare Bi-BiVO₄ by V leaching in a strongly basic solution. Again, the top and bottom hydrated BiVO₄ slabs shown in **Figure 6b** are slightly different. We note that the range of fluctuations of the CBM and VBM observed in our FPMD for the hydrated Bi-BiVO₄ (0.3 eV) is larger than that of the hydrated s-BiVO₄ (0.1 eV), as indicated in **Figure 5a**.

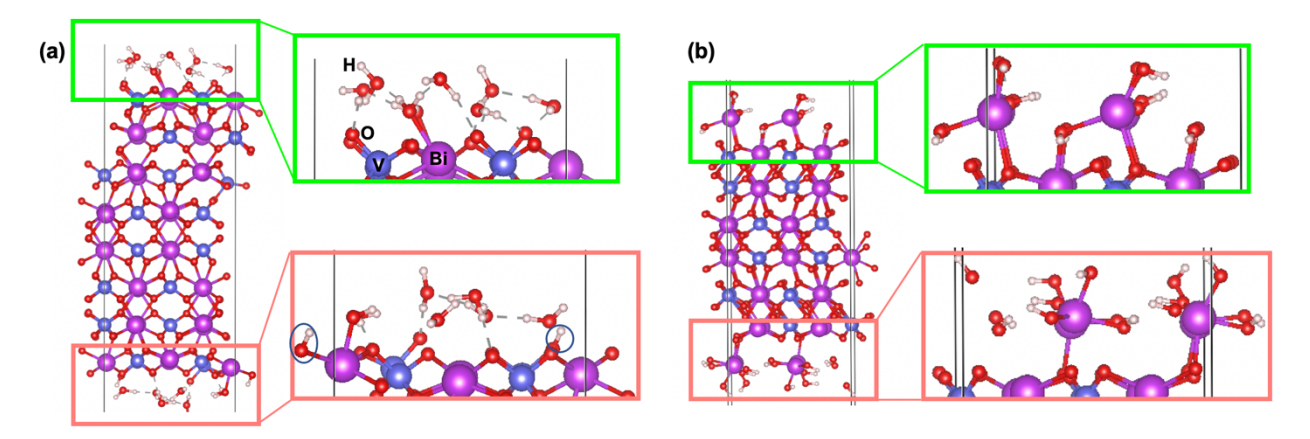


Figure 6. Atomistic models of hydrated (a) s-BiVO₄ and (b) Bi-BiVO₄ surfaces, as obtained from FPMD simulations at 330 K using the SCAN functional. One representative snapshot was extracted from the simulations and then further optimized with the PBE+U functional at 0 K. The hydrated configurations are not identical on the top and bottom surfaces of s-BiVO₄ and Bi-BiVO₄ slabs, as at finite T different configurations are sampled in FPMD. The blue circles at the bottom hydrated surface of s-BiVO₄ show hydroxylated Bi resulting from occasional dissociative water

adsorption on s-BiVO₄. Color scheme for the spheres in the figure: purple: bismuth; blue: vanadium; red: oxygen; white: hydrogen.

In the case of BiVO₄(010) with a dry surface, the band edges of Bi-BiVO₄ are much closer to the vacuum level than those of s-BiVO₄, as reported previously.⁴ (The fact that the VBM of Bi-BiVO₄ is closer to the vacuum was experimentally confirmed, ⁴ although the difference is not as significant as the difference computationally predicted based on theoretical models with limited slab size and atomic coordinations as discussed below.) When hydrated, the band edges of s-BiVO₄ move closer to the vacuum level while the band edges of Bi-BiVO₄ move away from the vacuum level (Figure 5a). We note that the dry and hydrated surface models considered here are to be used to construct a set of representative interfaces with FeOOH (discussed below) to demonstrate the effect of surface composition and the nature of the interfacial bonding on the interfacial band alignment in a qualitative manner. They are meant to show trends on band edge positions and not the prediction of exact values. The limitation of our computation for precisely predicting band edge positions comes from the limited slab size of the surface models used in our calculations as well as from specific atomic coordinations and compositions (e.g., we only considered 100% Bi with a specific local coordination for the Bi-rich surface) used for computation that may not accurately represent all the configurations present in experimental samples. Importantly, the band edge positions of the hydrated surfaces shown in Figure 5a are not meant for a quantitative comparison with the band edge positions of BiVO₄ photoanodes operating in aqueous media; such a comparison would require carrying out electronic structure calculations using atomistic models inclusive of bulk water, not just one hydration layer. The effect of adding bulk water (i.e., explicitly adding multiple, diffusing water molecules) at the interface of BiVO₄ photoanodes will be discussed in a forthcoming paper reporting in detail on solvation effects. Here we focus instead on interfacial models and relative band alignments at the BiVO₄/FeOOH interface.

To model the FeOOH layer, we used the crystal structure of γ -FeOOH. This choice stems from the fact that although the FeOOH layer in our experimental samples is too thin or amorphous to be detected by XRD, the Raman spectrum of the FeOOH sample prepared by a similar method resembles that of γ -FeOOH. Thus, γ -FeOOH is a reasonable structural model to understand our experimental samples. Considering the 2D nature of the γ -FeOOH structure, we expect that γ -FeOOH is most likely deposited with the layer parallel to the BiVO₄ surface exposing the (010) surface (see insets in **Figure 5b** for the crystal orientation). Thus, the (010) surface would best represent the surface in contact with BiVO₄, although it should be kept in mind that variations in orientation can exist in the real amorphous sample. In **Figure 5b**, we also included the band edge positions of the (100) facet as we find them to be farthest away from those of the (010) surface, making them good comparison points. For FeOOH, only dry surfaces were considered as the FeOOH layer naturally contains -OH groups on the surfaces, which cannot be further hydroxylated when water molecules are introduced. As in the case of BiVO₄ surfaces, it is to be expected that FeOOH band edge positions might also be influenced by local solvation effects and temperature fluctuations when bulk water is added at finite T.

The band alignments after contact between s-BiVO₄ or Bi-BiVO₄ and FeOOH are shown in **Figure 7**, where we considered two interfacial bonding models for s-BiVO₄/FeOOH and Bi-BiVO₄/FeOOH. In the first model (**Figure 7a,c**), the (s-, Bi-)BiVO₄/FeOOH interfaces are constructed by forming ionic bonds with bridging oxide ions (i.e., V/Bi-O-Fe) between the two phases. This type of interface can be obtained if water or hydroxyl groups on the hydrated BiVO₄

surface are replaced by O-Fe bonds when FeOOH is deposited on BiVO₄. Because the resulting interfacial models would resemble the interfaces formed by contacting the dry BiVO₄ surfaces with FeOOH, the dry surface models of BiVO₄ discussed in Figure 5a are used to construct the (s-, Bi-)BiVO₄/FeOOH interfaces shown in Figure 7 a,c. In the second model (Figure 7b,d), the (s-, Bi-)BiVO₄/FeOOH interfaces are made by forming hydrogen bonds between the two phases. This type of interface can be obtained if an FeOOH layer is deposited on BiVO₄ while preserving the hydrated BiVO₄ surface structure. In this case, as the BiVO₄ surface remains hydrated, the hydrated BiVO₄ surface models discussed in Figures 5a and 6 are used to construct the BiVO₄/FeOOH interfaces shown in Figure 7b,d.

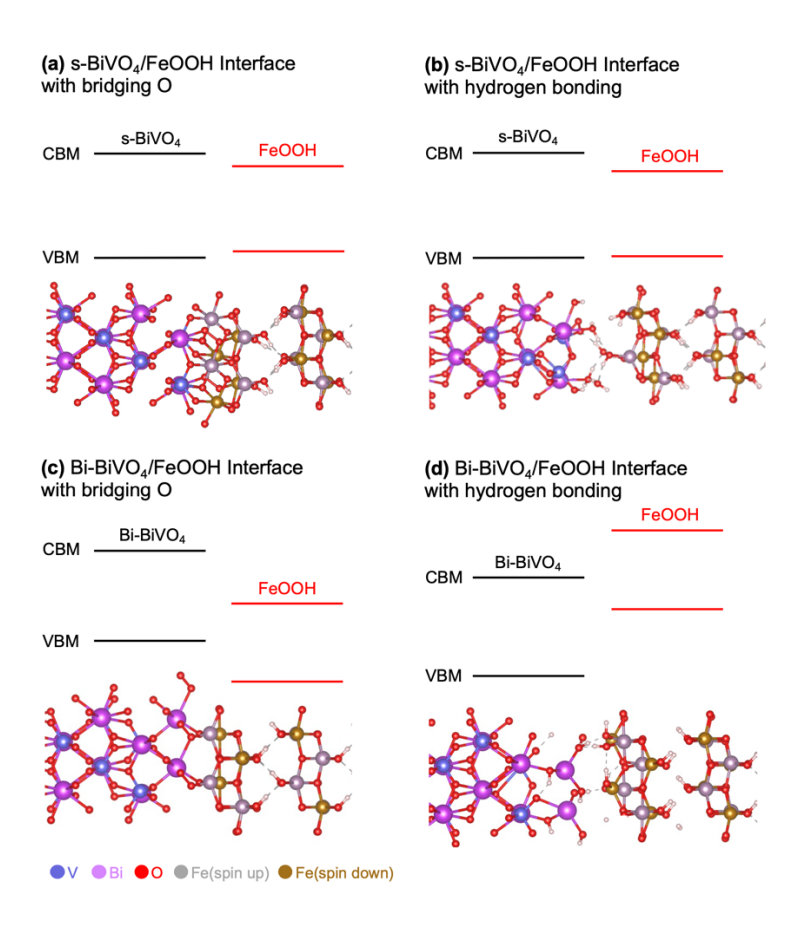


Figure 7. Band alignment between BiVO₄ and FeOOH model structures after contact and the corresponding atomistic structures of the interface, as obtained from PBE+U calculations (a) s-BiVO₄/FeOOH interfaced with bridging O, (b) s-BiVO₄/FeOOH interfaced with hydrogen bonding, (c) Bi-BiVO₄/FeOOH interfaced with bridging O, and (d) Bi-BiVO₄/FeOOH interfaced with hydrogen bonding.

The band alignment results shown in **Figure 7** for each case were obtained from electronic structure calculations on optimized slab atomic geometries. We note that in these calculations of the BiVO₄/FeOOH interface, the position of the Fermi level and the atomic positions are determined self-consistently and there is no a priori assumption on the position of the Fermi level. Geometry optimizations, carried out at the DFT level, ensure energetic equilibrium between the

two materials, and hence the proper alignment of the Fermi level. The band edge alignments were obtained by computing the local density of states (LDOS) in the direction perpendicular to the interface.^{29,30} We also verified that the same qualitative band alignments are obtained by using the electrostatic potential line-up method,²⁸ as explained in detail in the methods section

In the case of the s-BiVO₄/FeOOH interface with bridging oxygen ions, we considered four different ionic bonding configurations (e.g., different bond lengths and bond angles) (see Figure S3 for the detailed atomic structures) and found that they all result in a Type I band alignment shown in Figure 7a. In this alignment, the CBM and VBM of s-BiVO₄ straddle the CBM and VBM of FeOOH. Such a band alignment is not favorable for efficient interfacial electron-hole separation because photogenerated electrons as well as photogenerated holes can be transferred from BiVO₄ to FeOOH, leading to a recombination loss of holes in the FeOOH layer. In the case of the s-BiVO₄/FeOOH interface with hydrogen bonds (Figure 7b), the CBM of BiVO₄ is also higher than that of FeOOH, the VBMs of the two phases become very close to each other, meaning both electron transfer and hole transfer from s-BiVO₄ to FeOOH are possible under the open circuit condition. Thus, in either case, selective hole transfer from s-BiVO₄ to FeOOH in BiVO₄/FeOOH is not possible, which is unfavorable for BiVO₄/FeOOH that serves as a photoanode. These results explain the experimentally observed XPS results (i.e., no considerable change in the Fe²⁺: Fe³⁺ ratio in FeOOH under illumination) and J-V experiments (i.e., more positive photocurrent onset and less anodic photocurrent for OER). We show only qualitative band alignments in Figure 7 because the exact band positions of FeOOH are extremely sensitive to small variations of the atomic structure (e.g., strain conditions) in FeOOH.

In the case of the Bi-BiVO₄/FeOOH interface formed with bridging oxygen ions (Figure 7c), the calculated CBM and VBM of BiVO₄ are higher than those of FeOOH. This will allow for only electron transfer from BiVO₄ to FeOOH. Knowing experimentally that Bi-BiVO₄/FeOOH serves as a more efficient photoanode than s-BiVO₄/FeOOH, this theoretical model is not compatible with the experimental sample. Thus, we conclude that the experimental Bi-BiVO₄/FeOOH sample is not formed with bridging oxygen ions. In the case of the Bi-BiVO₄/FeOOH interface formed with hydrogen bonds (Figure 7d), a Type II band alignment is obtained. In this alignment, both the CBM and VBM of Bi-rich BiVO₄ are lower than those of FeOOH, enabling only hole transfer from Bi-BiVO₄ to FeOOH. This interfacial model can explain the experimentally observed XPS results (i.e., more Fe³⁺ formation in FeOOH under illumination due to facile hole transfer from BiVO₄) and J-V plots (i.e., more negative photocurrent onset and greater OER photocurrent) of the Bi-BiVO₄/FeOOH photoelectrode. When we computed formation energies of s-BiVO₄/FeOOH and Bi-BiVO₄/FeOOH interfaced with bridging oxygen ions and with hydrogen bonds, we found that the hydrogen bonded interfaces are more stable for both s-BiVO₄/FeOOH and Bi-BiVO₄/FeOOH (calculation details in the SI). Overall, our combined results suggest that when Bi-BiVO₄/FeOOH is assembled by photoelectrochemically depositing FeOOH on Bi-BiVO₄ in aqueous media, an FeOOH layer is added on the hydrated BiVO₄ surface forming hydrogen bonds and this interfacial bonding nature plays an important role in allowing for selective hole transfer from Bi-BiVO₄ to FeOOH, enabling a more efficient photon-tophotocurrent conversion for OER.

Conclusions

In summary, we have assembled s-BiVO₄(010)/FeOOH and Bi-BiVO₄(010)/FeOOH photoanodes with the only difference being the interfacial Bi:V ratio to investigate the impact of

the interfacial composition and structure on interfacial charge transfer. While the two photoanodes contain the same semiconductor and OEC, they show remarkably different photoelectrochemical performances for OER. The AP-XPS results obtained under illumination in the presence of water under the open circuit condition indicate that selective hole transfer from s-BiVO₄ to FeOOH does not occur at the s-BiVO₄/FeOOH interface. In contrast, hole transfer from Bi-BiVO₄ to FeOOH is promoted at the Bi-BiVO₄/FeOOH interface. The strikingly different OER photocurrent and AP-XPS results indicate that the surface composition of BiVO₄ considerably affects the band alignments at the BiVO₄/FeOOH interfaces. The computational studies revealed that the band alignments at the s-BiVO₄/FeOOH interface are such that electrons as well as holes can be transferred from s-BiVO₄ to FeOOH regardless of the bonding type between s-BiVO₄ and FeOOH, which explains why the anodic photocurrent onset of the s-BiVO₄/FeOOH photoanode for OER appears at a more positive potential. On the other hand, when the Bi-BiVO₄ surface forms an interface with FeOOH through hydrogen bonds, a Type II band alignment is achieved, allowing for selective hole transfer from Bi-BiVO₄ to FeOOH. These results explain why the Bi-BiVO₄/FeOOH photoanode suffers less from interfacial recombination and generates higher photocurrent for OER than the s-BiVO₄/FeOOH photoanode at any given potential. This study demonstrates for the first time the impact of the photoelectrode composition in the outermost layer and the bonding type between photoelectrode and catalyst on the interfacial band alignments. Our results also show that even for the same photoelectrode/catalyst pair, it is possible to deliberately tune the interfacial composition and structure to enhance desired interfacial charge transfer.

ASSOCIATED CONTENT

Supporting Information

The Supporting Information is available free of charge on the ACS Publication website: SEM images and Bi 4f XPS spectra of (s-, Bi-)BiVO₄/FeOOH and four different atomistic models of the s-BiVO₄/FeOOH interface formed with bridging oxygen ions (PDF).

AUTHOR INFORMATION

Corresponding Author

*Email: kschoi@chem.wisc.edu *Email: gagalli@uchicago.edu

*Email: mzliu@bnl.gov

Notes

The authors declare no competing interests.

Acknowledgements

This work was supported by the National Science Foundation (NSF) under grant no. CHE-2054986. This research used Materials Synthesis & Characterization and Proximal Probes facilities of the Center for Functional Nanomaterials, which is a U.S. DOE Office of Science

Facility, at Brookhaven National Laboratory under Contract No. DE-SC0012704. This research also used computational resources of the University of Chicago's Research Computing Center. Some of our simulations used codes developed within the MICCoM center, a Computational Materials Science Center funded by DOE/BES.

References

- (1) Nozik, A. J. Photoelectrochemistry: Applications to Solar Energy Conversion. *Annu. Rev. of Phys. Chem.* **1978**, *29*, 189–222.
- (2) Grätzel, M. Photoelectrochemical Cells. *Nature* **2001**, *414*, 338–344.
- (3) Walter, M. G.; Warren, E. L.; McKone, J. R.; Boettcher, S. W.; Mi, Q.; Santori, E. A.; Lewis, N. S. Solar Water Splitting Cells. *Chem. Rev.* **2010**, *110*, 6446–6473.
- (4) Lee, D.; Wang, W.; Zhou, C.; Tong, X.; Liu, M.; Galli, G.; Choi, K.-S. The Impact of Surface Composition on the Interfacial Energetics and Photoelectrochemical Properties of BiVO₄. *Nat. Energy* **2021**, *6*, 287–294.
- (5) Kim, T. W.; Choi, K.-S. Nanoporous BiVO₄ Photoanodes with Dual-Layer Oxygen Evolution Catalysts for Solar Water Splitting. *Science* **2014**, *343*, 990–994.
- (6) NIST X-ray Photoelectron Spectroscopy Database, NIST Standard Reference Database Number 20, National Institute of Standards and Technology, Gaithersburg MD, 20899 (2000), (accessed 2023-09-05).
- (7) Lu, J.-B.; Cantu, D. C.; Nguyen, M.-T.; Li, J.; Glezakou, V.-A.; Rousseau, R. Norm-Conserving Pseudopotentials and Basis Sets To Explore Lanthanide Chemistry in Complex Environments. *J. Chem. Theory Comput.* **2019**, *15*, 5987–5997.
- (8) Biesinger, M. C.; Payne, B. P.; Grosvenor, A. P.; Lau, L. W. M.; Gerson, A. R.; Smart, R. St. C. Resolving Surface Chemical States in XPS Analysis of First Row Transition Metals, Oxides and Hydroxides: Cr, Mn, Fe, Co and Ni. *Appl. Surf. Sci.* **2011**, *257*, 2717–2730.
- (9) Lin, T.-C.; Seshadri, G.; Kelber, J. A. A Consistent Method for Quantitative XPS Peak Analysis of Thin Oxide Films on Clean Polycrystalline Iron Surfaces. *Appl. Surf. Sci.* **1997**, 119, 83–92.
- (10) Perdew, J. P.; Burke, K.; Ernzerhof, M. Generalized Gradient Approximation Made Simple. *Phys. Rev. Lett.* **1996**, *77*, 3865–3868.
- (11) Giannozzi, P.; Andreussi, O.; Brumme, T.; Bunau, O.; Buongiorno, M.; Calandra, M.; Car, R.; Cavazzoni, C.; Ceresoli, D.; Cococcioni, M.; Colonna, N.; Carnimeo, I.; Corso, A. D.; de Gironcoli, S.; Delugas, P.; Jr, R. A. D.; Ferretti, A.; Floris, A.; Fratesi, G.; Fugallo, G.; Gebauer, R.; Gerstmann, U.; Giustino, F.; Gorni, T.; Jia, J.; Kawamura, M.; Ko, H.-Y.; Kokalj, A.; Marsili, M.; Marzari, N.; Mauri, F.; Nguyen, N. L.; Nguyen, H.-V.; Otero-de-la-Roza, A.; Paulatto, L.; Ponc, S.; Santra, B.; Schlipf, M.; Seitsonen, A. P.; Smogunov, A.; Timrov, I.; Thonhauser, T.; Umari, P.; Vast, N.; Wu, X.; Baroni, S. Advanced Capabilities for Materials Modelling with Quantum ESPRESSO. *J. Phys.: Condens. Matter* 2017, 29, 31.
- (12) Giannozzi, P.; Baroni, S.; Bonini, N.; Calandra, M.; Car, R.; Cavazzoni, C.; Ceresoli, D.; Chiarotti, G. L.; Cococcioni, M.; Dabo, I.; Corso, A. D.; de Gironcoli, S.; Fabris, S.; Fratesi, G.; Gebauer, R.; Gerstmann, U.; Gougoussis, C.; Kokalj, A.; Lazzeri, M.; Martin-Samos, L.; Marzari, N.; Mauri, F.; Mazzarello, R.; Paolini, S.; Pasquarello, A.; Paulatto, L.; Sbraccia, C.; Scandolo, S.; Sclauzero, G.; Seitsonen, A. P.; Smogunov, A.; Umari, P.; Wentzcovitch, R. M. QUANTUM ESPRESSO: A Modular and Open-Source Software Project for Quantum Simulations of Materials. *J. Phys.: Condens. Matter* **2009**, *21*, 395502.
- (13) Hamann, D. R. Optimized Norm-Conserving Vanderbilt Pseudopotentials. *Phys. Rev. B* **2013**, 88, 085117.
- (14) Schlipf, M.; Gygi, F. Optimization Algorithm for the Generation of ONCV Pseudopotentials. *Comput. Phys. Commun.* **2015**, *196*, 36–44.

- (15) Cococcioni, M.; de Gironcoli, S. Linear Response Approach to the Calculation of the Effective Interaction Parameters in the LDA + U Method. *Phys. Rev. B* **2005**, *71*, 035105.
- (16) Wang, W.; Strohbeen, P. J.; Lee, D.; Zhou, C.; Kawasaki, J. K.; Choi, K.-S.; Liu, M.; Galli, G. The Role of Surface Oxygen Vacancies in BiVO₄. *Chem. Mater.* **2020**, *32*, 2899–2909.
- (17) Cornell, R. M.; Schwertmann, U. *The Iron Oxides: Structure, Properties, Reactions, Occurences and Uses*, 1st ed.; Wiley, 2003.
- (18) Otte, K.; Pentcheva, R.; Schmahl, W. W.; Rustad, J. R. Pressure-Induced Structural and Electronic Transitions in FeOOH from First Principles. *Phys. Rev. B* **2009**, *80*, 205116.
- (19) Johnson, C. E. Antiferromagnetism of γ FeOOH: A Mossbauer Effect Study. *J. Phys. C: Solid State Phys.* **1969**, *2*, 1996.
- (20) Guo, H.; Barnard, A. S. Modeling the Iron Oxides and Oxyhydroxides for the Prediction of Environmentally Sensitive Phase Transformations. *Phys. Rev. B* **2011**, *83*, 094112.
- (21) Alexandrov, V.; Rosso, K. M. Electron Transport in Pure and Substituted Iron Oxyhydroxides by Small-Polaron Migration. *J. Chem. Phys.* **2014**, *140*, 234701.
- (22) Sun, J.; Ruzsinszky, A.; Perdew, J. P. Strongly Constrained and Appropriately Normed Semilocal Density Functional. *Phys. Rev. Lett.* **2015**, *115*, 036402.
- (23) Wang, W.; Favaro, M.; Chen, E.; Trotochaud, L.; Bluhm, H.; Choi, K.-S.; van de Krol, R.; Starr, D. E.; Galli, G. Influence of Excess Charge on Water Adsorption on the BiVO4(010) Surface. *J. Am. Chem. Soc.* **2022**, *144*, 17173–17185.
- (24) Ambrosio, F.; Wiktor, J.; Pasquarello, A. PH-Dependent Surface Chemistry from First Principles: Application to the BiVO₄ (010)–Water Interface. *ACS Appl. Materials & Interfaces* **2018**, *10*, 10011–10021.
- (25) Oshikiri, M.; Boero, M. Water Molecule Adsorption Properties on the BiVO₄ (100) Surface. *J. Phys. Chem. B* **2006**, *110*, 9188–9194.
- (26) Therrien, F.; Graf, P.; Stevanović, V. Matching Crystal Structures Atom-to-Atom. *J. Chem. Phys.* **2020**, *152*, 074106.
- (27) Pham, T. A. Predictive Theory and Modelling of Heterogeneous Interfaces. Ph.D., University of California, Davis, United States -- California. (accessed 2023-07-10).
- (28) Van de Walle, C. G.; Martin, R. M. Theoretical Study of Band Offsets at Semiconductor Interfaces. *Phys. Rev. B* **1987**, *35*, 8154–8165.
- (29) Yamasaki, T.; Kaneta, C.; Uchiyama, T.; Uda, T.; Terakura, K. Geometric and Electronic Structures of SiO₂/Si(001) Interfaces. *Phys. Rev. B* **2001**, *63*, 115314.
- (30) Anh Pham, T.; Li, T.; Nguyen, H.-V.; Shankar, S.; Gygi, F.; Galli, G. Band Offsets and Dielectric Properties of the Amorphous Si₃N₄/Si(100) Interface: A First-Principles Study. *Appl. Phys. Lett.* **2013**, *102*, 241603.
- (31) Huang, Z.; Han, F.; Li, M.; Zhou, Z.; Guan, X.; Guo, L. Which Phase of Iron Oxyhydroxides (FeOOH) Is More Competent in Overall Water Splitting as a Photocatalyst, Goethite, Akaganeite or Lepidocrocite? A DFT-Based Investigation. *Comput. Mater. Sci.* **2019**, *169*, 109110.
- (32) Zhan, J. AbinitioToolKit (Version 0.0.1) [Computer Software]., 2023. https://github.com/JiaweiZhan/abinitioToolKit
- (33) Park, Y.; McDonald, K. J.; Choi, K.-S. Progress in Bismuth Vanadate Photoanodes for Use in Solar Water Oxidation. *Chem. Soc. Rev.* **2013**, *42*, 2321–2337.
- (34) Zhang, W.; Yan, D.; Li, J.; Wu, Q.; Cen, J.; Zhang, L.; Orlov, A.; Xin, H.; Tao, J.; Liu, M. Anomalous Conductivity Tailored by Domain-Boundary Transport in Crystalline Bismuth Vanadate Photoanodes. *Chem. Mater.* **2018**, *30*, 1677–1685.

- (35) Brongersma, H. H.; Draxler, M.; de Ridder, M.; Bauer, P. Surface Composition Analysis by Low-Energy Ion Scattering. *Surf. Sci. Rep.* **2007**, *62*, 63–109.
- (36) Cushman, C. V.; Brüner, P.; Zakel, J.; Major, G. H.; Lunt, B. M.; Smith, N. J.; Grehl, T.; Linford, M. R. Low Energy Ion Scattering (LEIS). A Practical Introduction to Its Theory, Instrumentation, and Applications. *Anal.* **2016**, *8*, 3419–3439.
- (37) Zou, S.; Burke, M. S.; Kast, M. G.; Fan, J.; Danilovic, N.; Boettcher, S. W. Fe (Oxy)Hydroxide Oxygen Evolution Reaction Electrocatalysis: Intrinsic Activity and the Roles of Electrical Conductivity, Substrate, and Dissolution. *Chem. Mater.* **2015**, *27*, 8011–8020.
- (38) Seabold, J. A.; Choi, K.-S. Efficient and Stable Photo-Oxidation of Water by a Bismuth Vanadate Photoanode Coupled with an Iron Oxyhydroxide Oxygen Evolution Catalyst. *J. Am. Chem. Soc.* **2012**, *134*, 2186–2192.
- (39) Spray, R. L.; Choi, K.-S. Photoactivity of Transparent Nanocrystalline Fe₂O₃ Electrodes Prepared via Anodic Electrodeposition. *Chem. Mater.* **2009**, *21*, 3701–3709.
- (40) McDonald, K. J.; Choi, K.-S. A New Electrochemical Synthesis Route for a BiOI Electrode and Its Conversion to a Highly Efficient Porous BiVO₄ Photoanode for Solar Water Oxidation. *Energy Environ. Sci.* **2012**, *5*, 8553–8557.
- (41) Lee, D. K.; Choi, K.-S. Enhancing Long-Term Photostability of BiVO₄ Photoanodes for Solar Water Splitting by Tuning Electrolyte Composition. *Nat. Energy* **2018**, *3*, 53–60.
- (42) Govindaraju, G. V.; Wheeler, G. P.; Lee, D.; Choi, K.-S. Methods for Electrochemical Synthesis and Photoelectrochemical Characterization for Photoelectrodes. *Chem. Mater.* **2017**, *29*, 355–370.

TOC Graphic

